1   Revision 1
2
3
4
5
6
7
8

9   **Al and Si Diffusion in Rutile**

10
11
12

13   D.J. Cherniak*, E.B. Watson
14   Department of Earth and Environmental Sciences
15   Rensselaer Polytechnic Institute
16   Troy, NY 12180 USA

17
18
19
20
21
22
23
24
25
26
27
28
29
30
31
32
33
34
35
36
37
38

39   *Corresponding author:
40   D.J. Cherniak
41   Department of Earth & Environmental Sciences
42   Rensselaer Polytechnic Institute
43   Troy, NY 12180
44   chernd@rpi.edu

1

45

46 **Abstract**

47

48   Diffusion of Al and Si under anhydrous conditions has been measured in synthetic and natural

49   rutile. Experiments used Al_2O_3 or Al_2O_3-TiO_2 powder mixtures for Al diffusant sources, and

50   SiO_2-TiO_2 powder mixtures or quartz-rutile diffusion couples for Si. Experiments were run in air

51   in crimped Pt capsules, or in sealed silica glass ampoules with solid buffers (to buffer at NNO or

52   IW). Al profiles were measured with Nuclear Reaction Analysis (NRA) using the reaction

53   $^{27}Al(p, \gamma)^{28}Si$. Rutherford Backscattering Spectrometry (RBS) was used to measure Si diffusion

54   profiles, with RBS also used in measurements of Al to complement NRA profiles. We determine

55   the following Arrhenius relations from these measurements:

56

57   For Al diffusion parallel to c, for experiments buffered at NNO, over the temperature range

58   1100-1400ºC:

59       $D_{Al} = 1.21 \times 10^{-2} \exp(-531 \pm 27 \text{ kJ mol}^{-1}/RT) \text{ m}^2\text{s}^{-1}$

60

61   For Si diffusion parallel to c, for both unbuffered and NNO-buffered experiments, over the

62   temperature range 1100-1450ºC:

63       $D_{Si} = 8.53 \times 10^{-13} \exp(-254 \pm 31 \text{ kJ mol}^{-1}/RT) \text{ m}^2\text{s}^{-1}$

64

65   Diffusion normal to (100) is similar to diffusion normal to (001) for both Al and Si, indicating

66   little diffusional anisotropy for these elements. Diffusivities measured for synthetic and natural

67   rutile are in good agreement, indicating that these diffusion parameters can be applied in

68   evaluating diffusivities in rutile in natural systems Diffusivities of Al and Si for experiments

69   buffered at IW are faster (by a half to three-quarters of a log unit) than those buffered at NNO.

70   Si and Al are among the slowest-diffusing species in rutile measured thus far. Diffusivities of

71   Al and Si are significantly slower than diffusion of Pb, and slower than diffusion of tetravalent

72   Zr and Hf and pentavalent Nb and Ta. These data indicate that Al compositional information will

73   be strongly retained in rutile, providing evidence for the robustness of the recently developed Al

74   in rutile thermobarometer. For example, at 900°C, Al compositional information would be

75   preserved over ~3 Gyr in the center of 250 μm radius rutile grains, but Zr compositional

76   information would be preserved for only about 300,000 years at this temperature. Al-in-rutile

77   compositions will also be much better preserved during subsolidus thermal events subsequent to

78   crystallization than those for Ti-in-quartz and Zr-in-titanite crystallization thermometers.

79
80
81
82
83
84
85   Keywords: rutile, diffusion, aluminum, silicon, Rutherford Backscattering, Nuclear Reaction
86   Analysis, geothermometry, geobarometry
87
88
89
90

Introduction

91

92   Rutile, found in a variety of geological settings, can incorporate significant amounts of

93   trivalent, divalent and pentavalent cations, including several high-field strength elements, with

94   concentrations up to tens of percent (e.g., Vlassopoulos et al., 1993). The geochemical behavior

95   of these trace and minor elements in rutile can offer insight into subduction zone processes (e.g,

96   Ewing and Müntener, 2018; Ryerson and Watson, 1987; Zack et al., 2002; Brenan et al., 1994;

97   Stalder et al, 1998; Foley et al, 2000); HFSE with multiple valence states incorporated in rutile

98   also have the potential to provide information on fO_2 conditions (e.g., Liu et al., 2014; Guo et al.,

99   2017). Since rutile tends to remain stable during sedimentary and diagenetic processes, its trace

100   element signatures can reveal information about provenance (e.g. Zack, et la., 2002; Morton et

101   al., 1999), and may be used in geospeedometry (e.g., Cruz-Uribe et al., 2014; Kohn et al., 2016).

102   The Zr-in-rutile geothermobarometer (Degeling, 2003; Zack, et al., 2004b; Watson et al. 2006;

103   Tomkins et al. 2007) has been increasingly applied in a range of studies to assess crystallization

104   temperatures and/or pressures (e.g., Mitchell and Harley, 2017; Pape et al., 2016; Ewing et al.,

105   2013; Taylor-Jones and Powell, 2015; Tual et al., 2018). Rutile is also used as a U-Pb

106   geochronometer (e.g,, Corfu and Andrews, 1986; Corfu and Muir, 1989; Mezger et al., 1991;

107   1989; Schandl et al., 1990; Wong et al., 1991; Davis, 1997; Smye and Stockli, 2014).

108   In this work, we report results for Si and Al diffusion in natural and synthetic rutile, with

109   evaluation of the effects of oxygen fugacity and crystallographic orientation on diffusion. These

110   data supplement and complement earlier measurements of diffusion of trace and minor elements

111   in rutile, and may permit greater general understanding of diffusion-controlled processes in

112   rutile.

113   Most notably, recent experimental work (Hoff and Watson, 2018) has shown the potential for

114   use of Al concentrations in rutile as a geothermobarometer. Al concentrations in rutile may also

115   affect diffusion of other species, such as Cr (e.g., Sasaki et al., 1985). Taylor-Jones and Powell

116   (2015) have proposed that slow-diffusing Si in rutile may lead to the slowing of Zr diffusion,

117   resulting in higher retentivity of Zr and higher closure temperatures. However, Kohn et al.

118   (2016) have argued against the hypothesis of Zr coupling with slower-diffusing Si, asserting

119   instead that high Zr contents (and thus high Zr-in-rutile temperatures) observed in UHT rocks are

120   a consequence of the degree to which the surfaces of rutile crystals are able to maintain

121   equilibrium with matrix minerals, including zircon and baddeleyite. Despite possible

122   complexities in natural systems, measurements of Si diffusion in rutile are of value given the

123   ubiquity of silicon in geologic systems, as well as the utility of these diffusivities in

124   understanding processes such as the exsolution of zircon needles in rutile (e.g., Pepe et al, 2016).

125   Slightly reduced and doped rutiles, as semiconducting materials, have been used in a range of

126   technological applications. Al-doped rutile has been developed as an optical material (e.g, Hatta

127   et al. , 1996); Si can also be added to rutile to tailor optical properties (Gonzalez-Elipe et al,

128   2006; Demiryont, 1985). Al is a common additive to TiO_2 pigments to enhance photochemical

129   stability, and may have large effects on the conductivity of rutile and its polymorphs (Bak et al.,

130   2003), and on crystal growth and transformation kinetics (Gesenhues, 1997; Gesenhues and

131   Rentschler, 1999; Karvinen, 2003). Understanding diffusion of key dopant species in rutile can

132   assist in refining production processes and provide constraints on the long-term integrity of these

133   materials.

134

135

5

Experimental Procedure and Materials

The majority of diffusion experiments in this study were run on synthetic rutile. The synthetic

rutile, from the MTI Corporation, was purchased in the form of wafers polished on one side, in

either (001) or (100) orientation. To explore the effects of the presence of trace and minor

elements on diffusion, some Si diffusion experiments were run using a natural rutile. The natural

rutile, from Pennsylvania, was from the same specimen as used in our earlier studies of Pb, Hf

and Zr diffusion in rutile (Cherniak et al., 2007a; Cherniak, 2000). Minor and trace element

concentrations from LA-ICPMS analyses of the rutile (based on averages of 3 or 6 point analyses

on synthetic and natural rutile grains, respectively) are presented in Table 1. The wafers of

synthetic rutile were cut into square pieces, about 2 mm on a side. The natural rutile was cut

normal to c into slabs about 0.5 mm thick, polished with SiC papers and alumina powders down

to 0.3 μm, and finished with a chemical polish using colloidal silica.

Si diffusion experiments were conducted using quartz-rutile diffusion couples, or with powder

sources containing SiO_2. The powder sources used were either dried SiO_2 powder, or a mixture

of TiO_2 and SiO_2 powders in 3:1 (by wt.) ratio, ground under ethanol, dried, and heated in a Pt

crucible for one day at 1250°C. The SiO_2-TiO_2 powder sources worked well for experiments run

in air, but the buffered experiments run in sealed silica glass capsules showed significant Si-rich

material clinging to rutile sample surfaces following diffusion anneals, which precluded

successful analysis of these samples. As a consequence, only quartz-rutile diffusion couples were

used in buffered experiments.

For the Al diffusion experiments, sources of diffusant were Al_2O_3 powder, or mixtures of

TiO_2 and Al_2O_3 powders, in either 3:1 or 10:1 (by wt.) ratios. The TiO_2-Al_2O_3 powder mixtures

were ground under ethanol, dried, and heated in Pt crucibles for one day at 1250°C. To explore

6

159   potential effects of coupled substitutions on Al diffusion, an experiment was run which

160   incorporated Nb into the source material. For this source, the TiO_2-Al_2O_3 10:1 wt. ratio powder

161   mixture was combined with Nb_2O_5 powder in a weight ratio of 100:1.

162   For powder-source experiments, rutile crystals were surrounded by the source powders in Pt

163   capsules, and capsules crimped shut. Diffusion couples were created by placing polished faces of

164   rutile and synthetic quartz slabs in contact, tying the couple together with Pt wire, and wrapping

165   the couple in Pt mesh. For experiments run under buffered conditions, the Pt capsules or

166   diffusion couples were placed inside a silica glass ampoule with another crimped Pt capsule

167   containing the buffer material (mixtures of Ni metal and nickel oxide powders to buffer at NNO,

168   or FeO powder and Fe flakes to buffer at IW); silica glass chips were used to physically separate

169   the samples and buffer capsules inside the silica glass ampoule. The sample-buffer assemblies

170   were then sealed in the silica ampoule under vacuum.

171   All experiments were run in one-atmosphere tube furnaces with $MoSi_2$ heating elements, with

172   sample temperatures monitored by type S (Pt-Pt10%Rh) thermocouples with temperature

173   uncertainties of ~±2°C. Experiments were then removed from the furnace and allowed to cool in

174   air. The rutile crystals were extracted from capsules and cleaned ultrasonically in distilled H_2O

175   and ethyl alcohol. Experimental conditions and durations for Si and Al diffusion experiments

176   are presented in Tables 2 and 3.

177   Time-series studies were performed for both Al and Si diffusion in order to establish that the

178   measured concentration profiles are due to volume diffusion and are not a result of other

179   processes such as surface reaction that could lead to enhanced concentrations of the diffusant in

180   the near-surface region. For these time series, a set of Si diffusion experiments was performed at

7

181   1300°C for experiments ranging from 19 hours to one week in duration, and a set of Al diffusion

182   experiments at 1250°C for 1 to 6 days.

183

184   **Nuclear Reaction Analysis (NRA) of Al**

185   The Al diffusion experiments were analyzed using nuclear reaction analysis (NRA) with the

186   reaction $^{27}Al(p,\gamma)^{28}Si$. These analyses were performed at the Ion Beam Laboratory at the

187   University at Albany, using proton beams produced by the Dyamitron accelerator. For Al

188   profiling, the 992 keV resonance of the reaction was employed, with a bismuth germanate

189   (BGO) detector used to detect gamma rays produced in the reaction (Cherniak, 1995; Cherniak

190   and Watson, 1992; Tailby et al., 2018). Energy steps of 1.0 - 0.5 keV for the incident proton

191   beam were taken near the resonance energy to profile Al at depths near the sample surface, with

192   larger energy steps (2-5 keV) at greater depths (above ~150 nm). Spectra from untreated

193   specimens of rutile were also recorded at each energy step to evaluate background levels in the

194   gamma energy region of interest, and gamma spectra of Al foil were collected as a standard to

195   convert gamma yields into Al concentrations for rutile samples. Typical detection limit for

196   analytical conditions used in this work is ~100 ppm atomic. Depth scales for the Al profiles were

197   calculated from the energy difference between the incident proton beam and the resonance

198   energy, and by the stopping power (energy loss of the protons as a function of depth in the

199   material); stopping powers used in depth calculations were determined with the software SRIM

200   (Ziegler and Biersack, 2006).

201

202   **RBS analysis**

8

203   Si diffusion experiments were analyzed with RBS. In addition, Al diffusion experiments were

204   measured with RBS to complement the NRA analyses described above. RBS has been used as

205   the primary analytical method in many of our diffusion studies, including measurements of Pb,

206   Zr and Hf diffusion in rutile (Cherniak et al., 2007a; Cherniak, 2000). The analytical procedures

207   used here are similar, with a $^4\text{He}^+$ incident beam of 2 or 3 MeV energy used for analysis. RBS

208   spectra were converted to Si and Al concentration profiles using procedures similar to those

209   described in other work (e.g., Cherniak, 1993). Si (and Al) signals rest on those from He

210   backscattered from Ti in the sample, resulting in high backgrounds, so detection limits are on

211   order of a few tenths of an atomic percent, but Si concentrations are relatively high in the

212   samples (up to a few % atomic, at the highest temperatures of the experiments), so peaks can be

213   well-resolved from background signals. For Al, in cases where both RBS and NRA

214   measurements of samples were made (as discussed below), diffusivities agreed within

215   experimental uncertainties.

216

217   **Fitting of Depth Profiles**

218   RBS and NRA depth profiles were fit with a model to determine the diffusion coefficient (D).

219   Diffusion is modeled as simple one-dimensional, concentration independent diffusion in a semi-

220   infinite medium with a source reservoir maintained at constant concentration (i.e., a

221   complementary error function solution). The rationale for the use of this model has been

222   discussed in previous publications (e.g., Cherniak and Watson, 1992). Diffusivities are evaluated

223   by plotting the inverse of the error function (i.e., $erf^{-1}((C_o - C(x,t))/C_o)$) vs. depth ($x$) in the

224   sample. A straight line of slope $(4Dt)^{-1/2}$ results if the data conform to a complementary error

225   function solution. C_o, the surface concentration of diffusant, is independently determined by

9

226   iteratively varying its value until the intercept of the line converges on zero. In Figure 1, typical

227   diffusion profiles for both Al and Si are shown. The uncertainties in concentration and depth

228   from each data point (mainly derived from counting statistics and backgrounds in the former and

229   RBS detector resolution in the latter) were used to evaluate the uncertainties in the diffusivities

230   determined from the fits to the model.

231

232   **Results**

233   The results for Al diffusion are plotted in Figure 2 and presented in Table 2. Diffusivities

234   obtained with NRA and RBS agree within uncertainties. There is little evidence of diffusional

235   anisotropy. Al diffusion appears to have a weak negative dependence on oxygen fugacity, with

236   diffusivities under IW-buffered conditions about half a log unit higher than those under NNO-

237   buffered conditions. Samples run with the 3:1 TiO_2:Al_2O_3 source generally have higher surface

238   concentrations than samples run with the 10:1 source (typically 2-6x higher at a given

239   temperature under NNO-buffered conditions), but diffusivities agree within experimental

240   uncertainty. Surface concentrations of the diffusant also display a broad trend of increasing with

241   increasing temperature. For diffusion normal to (001), for experiments buffered at NNO, we

242   obtain an activation energy of 531 ± 27 kJ mol^{-1} and pre-exponential factor of 1.21×10^{-2} $m^2 s^{-1}$

243   ($\log D_o = -1.92 \pm 0.92$).

244   A time series at 1250°C, conducted for Al diffusion in rutile normal to (001), with

245   experiments run for times ranging from 24 hours to more than six days (Figure 4a), results in

246   diffusivities that are consistent within experimental uncertainty, providing evidence that volume

247   diffusion, rather than other phenomena such as surface reaction, is the dominant contributor to

248   the measured diffusion profiles over this range of conditions. No anomalously-shaped profiles

249   are observed for Al (or Si) that would be suggestive of concentration-dependence of diffusion,

250   and experiments with sources containing different concentrations of diffusant yield diffusivities

251   that agree within experimental uncertainty.

252   Diffusion data for Si are plotted in Figure 3 and presented in Table 3. For Si diffusion

253   perpendicular to (001) in synthetic rutile under unbuffered conditions, we obtain an activation

254   energy of 275 ± 45 kJ mol^{-1} and a pre-exponential factor 4.41×10^{-12} m^{2}s^{-1} (log D$_o$ = -11.36 $\pm$

255   1.38). There is little evidence of diffusional anisotropy when comparing diffusivities normal to

256   (100) and (001). For diffusion under NNO-buffered conditions in synthetic rutile, normal to

257   (001), an activation energy of 216 ± 48 kJ mol^{-1} and a pre-exponential factor 4.07×10^{-14} m^{2}s^{-1}

258   (log D$_o$ = -13.39 $\pm$ 1.62) are obtained. A fit to both the NNO- buffered and unbuffered data

259   results in an activation energy of 254 ± 31 kJ mol^{-1} and a pre-exponential factor 8.53×10^{-13} m^{2}s^{-1}

260   (log D$_o$ = -12.07 $\pm$ 1.03). Diffusivities of Si in natural rutile under NNO-buffered conditions do

261   not differ significantly from those obtained for NNO-buffered synthetic rutile, indicating that

262   differences in trace and minor element compositions between the synthetic and natural materials

263   have little effect on diffusion, a finding consistent with observations for Hf and Pb diffusion

264   (Cherniak, 2000; Cherniak et al. 2007a). Like Al, Si diffusion exhibits a negative dependence on

265   oxygen fugacity when comparing diffusivities under NNO- and IW-buffered conditions.

266   As with Al, a time series for Si diffusion in rutile normal to (001) was run, in this case at

267   1300°C for times ranging from 19 hours to a week (Figure 4b). Diffusivities are in agreement

268   within experimental uncertainties, suggesting that volume diffusion is the dominant contributor

269   to the observed Si diffusion profiles.

270

271

11

272 **Comparison with diffusivities of other elements in rutile and potential diffusion**

273 **mechanisms**

274

275   A summary of selected diffusion data for cations in rutile is plotted in Figure 5. Si and Al are

276 among the slowest-diffusing species in rutile measured to date. Si diffuses about 6 orders of

277 magnitude slower than Ti. Diffusivities of Al and Si are significantly lower than those of

278 divalent cations, including the large divalent cations Pb and Ba (Cherniak, 2000; Nakayama and

279 Sasaki, 1963) and other trivalent cations, including Sc and Cr (Sasaki et al., 1985). Al and Si also

280 diffuse more slowly than tetravalent Zr and Hf and pentavalent Nb and Ta (Marschall et al.,

281 2013; Dohmen et al., 2018; Cherniak et al., 2007a). For example, Si diffusion is about 2 orders

282 of magnitude slower than the Zr diffusivities determined by Cherniak et al. (2007a), and about 3

283 orders of magnitude slower than Pb diffusion; Al diffusion is about 6 orders of magnitude slower

284 than Nb diffusion, and 9 orders of magnitude slower than Cr diffusion (Sasaki et al., 1985).

285   Trivalent and more highly charged cations, which may migrate via a coupled

286 interstitial/interstitialcy mechanism (Zhu et al., 2017), and divalent cations of large ionic radius

287 such as Ba (Nakayama and Sasaki, 1963) and Pb (Cherniak, 2000), do not show pronounced

288 diffusional anisotropy. This contrasts with the significant diffusional anisotropy of small divalent

289 cations, which travel interstitially through open channels in the rutile structure along the c-axis

290 (Sasaki et al., 1985), a mechanism consistent with findings from DFT calculations (Zhu et al.,

291 2017).

292   Al^{3+} predominately substitutes for Ti^{4+} on normal octahedral sites at lower pressures, but

293 higher pressures induce the incorporation of Al^{3+} into octahedral interstices of the rutile structure

294 (Escudero et al., 2012). Al solubility increases with increasing temperature (Stebbins, 2007) and

12

295   pressure, with 10 wt% Al_2O_3 in rutile at 1300°C and 7 GPa (Escudero et al., 2012), with

296   concentrations at 1-atm in the range of 1-2 wt% Al_2O_3 (Escudero et al., 2012; Slepetys and

297   Vaughan, 1969); these values are broadly consistent with surface concentrations determined for

298   the lower-temperature experiments using the 10:1 TiO_2:Al_2O_3 source. For samples with up to 1

299   wt % Al_2O_3, Al is found in ordered, isolated octahedral (Ti sites), while at higher concentrations,

300   Al predominates in disordered octahedral sites, with possible contributions from both Ti sites

301   with Al neighbors and interstitials (Stebbins, 2007). The substitution of Al in Ti sites may be

302   compensated for by oxygen vacancies (Hatta et al., 1996; Islam et al., 2007); while interstitial

303   substitutions are possible, substitution on Ti lattice sites is energetically favorable. The larger

304   size of Al compared with Si, along with the potential for migrating via defect complexes to

305   preserve local charge balance, may lead to the higher activation energy for diffusion observed for

306   Al. In contrast, because of its small size compared with Ti, Si may have an off-center position in

307   the rutile lattice, and may also occupy interstitial positions (Golden et al., 2015), which could

308   contribute to the lower activation energy for Si diffusion. As with Al, Si solubilities in rutile

309   increase with increasing temperature and pressure (Ren et al., 2009), with solubilities, for

310   example, of ~1.5 wt% at 10 GPa and 1800°C, and ~5 wt% at 2000°C and 23 GPa. While it is

311   difficult to extrapolate down to lower pressure and temperature conditions, about half of our Si

312   surface concentrations fall below the former value.

313   The influence of point defect chemistry on chemical diffusion in rutile is discussed in

314   numerous publications (e.g., Nowotny et al., 2006a;b; 2012). The principal atomic defects in

315   undoped rutile are titanium interstitials and oxygen and titanium vacancies (e.g., Marucco et al.,

316   1981; Hoshino et al., 1985; Bak et al., 2012). There are two kinetic regimes associated with the

317   diffusion-controlled equilibration kinetics of TiO_2 . The first is controlled by transport of rapidly

318   moving defects (oxygen vacancies, titanium interstitials) and the second is determined by the

319   transport of titanium vacancies which diffuse much more slowly; this results in a difference in

320   diffusivities between the two regimes of about 4 orders of magnitude (Nowotny et al., 2006a;b).

321   Additional point defects will be present if altervalent impurities reside on Ti sites in rutile.

322   Common substitutional impurities in natural rutile are the pentavalent cations Nb and Ta, ferric

323   and ferrous iron, as well as other transition elements and Al (Deer et al., 1992). Electrostatic

324   balance for pentavalent cations is commonly achieved by vacancies in cation sites, or by

325   complementary substitution of divalent or trivalent cations (such as Fe) on Ti lattice sites. The

326   pentavalent cations Ta and Nb diffuse much more rapidly than Al (Marschall et al., 2013;

327   Dohmen et al., 2018) and our results indicate that the presence of pentavalent cations as potential

328   charge compensating species appears to have little effect on Al diffusion. For divalent and

329   trivalent cations, charge compensation may be via oxygen vacancies or Ti interstitials.

330   Experimental and theoretical studies suggest that trivalent species such as Cr and Sc, and

331   tetravalent Zr are likely to diffuse via an interstitialcy mechanism that involves tetravalent

332   interstitial Ti ions (Sasaki et al., 1985; Zhu et al., 2017). The diffusion rates for these cations

333   (along with Ti self diffusion; e.g., Akse and Whitehurst, 1978) have a dependency on oxygen

334   fugacity to the negative one-fifth power ($D \propto (pO_2)^{-1/5}$), which provides supporting evidence for

335   tetravalent Ti interstitials as the controlling point defect. Recent work by Dohmen et al. (2018)

336   on diffusion of tetravalent (Zr, Hf) and pentavalent (Nb, Ta) cations in rutile has determined the

337   presence of two different diffusion mechanisms: (i) an interstitialcy mechanism involving

338   trivalent Ti on interstitial sites, and (ii) a vacancy mechanism involving Ti vacancies. The former

339   is dominant at lower fO_2 (< QFM +2 log units), as well as at high temperatures (above 1350°C),

14

340   and has a negative dependence on fO_2, with the latter the dominant mechanism at higher fO_2 (>

341   QFM+2) and having diffusivities largely independent of fO_2.

342   Both Si and Al diffusivities appear broadly consistent with a negative dependence on fO_2,

343   suggesting an interstitialcy mechanism. In contrast to Al, activation energies for diffusion of Si

344   are similar to those for Ti. While we do not have full understanding of lattice diffusion

345   mechanisms from the results of this study, the data reported are from experiments conducted

346   under conditions of geologic relevance. These results indicate that Al and Si diffusion are not

347   greatly affected by the differing amounts of minor and trace elements present in the synthetic and

348   natural rutiles. However, it is important to note that while Al and Si concentrations in these

349   experiments approach those that could be found in mantle-derived rutile, they are much higher

350   than concentrations generally found in crustal rutile, which range up to several hundred ppm

351   (e.g., Zack et al., 2004a). The present data, given the detection limits for analysis and the

352   relatively high concentrations of Al and Si in diffusion experiments, do not preclude the

353   occurrence of differing diffusion mechanisms at lower concentrations of Al and Si.

354   The effects of pressure, and water or other hydrous species on diffusion rates are also

355   considerations in applying these experimental results. Pressure effects on diffusion in rutile have

356   not been extensively explored, but they are unlikely to be large for geologically reasonable

357   pressure ranges. There has been some investigation of the effects of hydrous species on oxygen

358   diffusion (Moore et al., 1998), which indicates that oxygen diffusion in rutile grown in the

359   presence of water, or in rutile grains reduced in such an environment, is about an order of

360   magnitude slower than in rutile reduced under anhydrous conditions, but there is little evidence

361   to date of the influence of hydrous species on cation diffusion.

15

362   Although the potential effects of the factors of concentration and the presence of hydrous

363   species on Al and Si diffusion are not fully resolved, we apply our diffusion data (with the

364   caveats above) in simple calculations and comparisons in the sections that follow.

365   **Si and Al diffusion in other minerals compared with rutile**

366   A summary of data for Al and Si diffusion is plotted in Figure 6. As in rutile, Al diffusion in

367   Al_2O_3 has a high activation energy for diffusion, and diffusivities are comparable in magnitude

368   to those for rutile. Al diffusion is much faster in MgO, olivine, quartz, and magnetite. Si

369   diffusion in rutile is slower than quartz, MgO and labradorite, but faster than Si in zircon,

370   anorthite, and olivine, and comparable to silicate perovskite and diopside over the temperature

371   range under which experiments were conducted. However, given the differences in activation

372   energies for diffusion, Si diffusion in rutile will be faster than in most other minerals at lower

373   temperatures (below ~1000°C) with the exception of diopside and MgO.

374   Béjina and Jaoul (1997) found that diffusion parameters obtained for Si diffusion in silicates

375   conform to a linear compensation law when the activation energy for diffusion is plotted as a

376   function of the log of the pre-exponential factor. This compensation relation, using the data

377   tabulated in Bejina and Jaoul (1997), a few more recent results, including that for zircon from

378   Cherniak (2008), was described in Cherniak (2008) by the equation $E = 647.7 + 30.5*\log D_o$.

379   Béjina and Jaoul (1997) argue that compensation behavior may be explained by the 'strain

380   energy' model proposed in Zener (1952), in which the Gibbs free energy of diffusion is

381   considered the 'elastic work' required to place the defect in its excited state for migration within

382   the lattice. They note that differences in activation enthalpies among individual materials are

383   likely due to differences in the coupling of point defects that minimize the migration energy for

16

384   Si through the lattice, and/or the characteristic 'extrinsicity' of the material (based on its impurity

385   levels, non-stoichiometry, presence of aliovalent cations, and other factors).

386   Interestingly, our diffusion parameters for Si in rutile fall closely along the compensation

387   trend (Figure 7). If we interpret our findings in light of these observations, the relatively low

388   activation energy for Si diffusion in rutile may be in part attributable to the greater possibility of

389   non-stoichiometry of rutile and the potential for the coupling of point defects in ways that may

390   reduce the energies for Si migration through the mineral lattice (e.g., Bejina and Jaoul, 1997).

391   Diffusion parameters for Si in MgO (Sakaguchi et al., 1992) also fall along the compensation

392   trend. Whether this conformity to a diffusion compensation trend for Si diffusion applies to other

393   non-silicates remains unclear, but these results may be suggestive of a more generalized

394   applicability of the Meyer-Neldel Rule (diffusion compensation law) for Si diffusion. As Jones

395   (2014) has noted, when considering the case of a single diffusing species in a range of mineral

396   phases, it may be the case that those minerals with a large average activation barrier (high E_a)

397   compensate with increased frequency of attempts to diffuse (larger D_o) (e.g., Boisvert et al.,

398   1995), thus resulting in these diffusion compensation trends.

399

400   **Diffusion in mineral – element pairs used as geothermobarometers**

401   Figure 8 presents a summary of data for diffusion of mineral-element pairs employed in

402   crystallization geothermo(baro)meters. These mineral-element pairs include Zr in rutile

403   (Degeling, 2003; Zack et al., 2004b; Watson et al., 2006; Tomkins et al., 2007; Ferry and

404   Watson, 2007), Ti in zircon (Watson et al., 2006; Ferry and Watson, 2007, Watson and

405   Harrison, 2005), Ti in quartz (Wark and Watson, 2006; Thomas et al., 2010), and Zr in titanite

406   (Hayden et al., 2008), and Al in rutile (Hoff and Watson, 2018). The Al diffusion data from the

17

407   present work and measurements of diffusivities for the other mineral-element pairs (Cherniak,

408   2006; Cherniak et al., 2007a; b; Cherniak and Watson, 2007) can be used to evaluate the relative

409   resistance of these geothermometers to diffusional alteration when these mineral phases

410   experience subsolidus thermal events following crystallization. For comparison, we also plot our

411   data for Si diffusion.

412   Diffusion of Al in rutile is faster than Ti diffusion in zircon, but considerably slower than Ti

413   diffusion in quartz, and slower than Zr diffusion in titanite and rutile under geologically relevant

414   conditions. For example, at 800°C, Al diffusion in rutile would be about 5 orders of magnitude

415   faster than Ti diffusion in zircon, but 7 orders of magnitude slower than Ti diffusion in quartz,

416   and ~5 and 6 orders of magnitude slower than Zr diffusion in rutile and titanite, respectively.

417   At 800°C, Si would diffuse more slowly than Zr in rutile by about 2 orders of magnitude.

418   Although slower diffusivities of Si with respect to Zr in rutile are unlikely to influence

419   temperatures derived from Zr-in-rutile thermometry (Kohn et al., 2016), Si diffusion may be

420   rate-limiting for other processes, such as the exsolution of zircon needles in rutile. Also, Si is a

421   significant trace component of natural rutile whose concentration has been shown to be

422   particularly sensitive to pressure (Gaetani et al., 2008; Ren et al., 2009; Mosenfelder et al., 2010;

423   Escudero and Langenhorst, 2012). Based in part on the data of Gaetani et al. (2008), Taylor-

424   Jones and Powell (2015) proposed a preliminary equation to describe the T and P dependence of

425   Si uptake in rutile in equilibrium with quartz and zircon. A comprehensive experimental

426   calibration may emerge in the foreseeable future, which would elevate the importance of our new

427   diffusion law for Si to a new level. Taylor-Jones and Powell (2015) emphasized the potential

428   value of a high closure temperature (T_C) for Si diffusion in rutile, contrasting with the relatively

429   low T_C value for Zr diffusion (see next section).

18

430   The relatively low diffusivity of Al indicates that the Al-in-rutile geothermobarometer (Hoff

431   and Watson, 2018) will be resistant to diffusional resetting under a broad range of geologic

432   conditions. In the following section, we will evaluate time-temperature scenarios under which

433   these records may be preserved or compromised.

434

435   **Preservation of chemical signatures for various crystallization thermometers**

436   Using the diffusion data reported in this work, we can illustrate how well specific

437   crystallization geothermometers may preserve past temperatures with calculations that constrain

438   conditions under which resetting of Al, Si, Zr or Ti chemical signatures (and therefore

439   information about crystallization temperatures) may take place. For a simple example, we use a

440   model in which the mineral grains are spheres of radii a having an initial uniform concentration

441   of diffusant C_1, which are exposed to an external medium with diffusant concentration C_o. Based

442   on these initial and boundary conditions, a solution to the diffusion equation at the center of the

443   spheres can be derived (e.g., Crank, 1975). For circumstances when the dimensionless parameter

444   Dt/a^2 (where D is the diffusion coefficient and t is the time) has a value than or equal to 0.03, the

445   concentration at the center of the sphere will remain unchanged from the initial value. This can

446   be referred to as a "center retention" criterion. At greater values of Dt/a^2 , concentrations of

447   diffusant at the sphere's center will be is affected by the external concentration C_o. If we

448   consider an infinite cylinder geometry (better suited for many rutile grains), a similar model can

449   be applied with a as the radius of the cylinder; for this model the relevant value of the center-

450   retention parameter Dt/a^2 is ∼ 0.04.

451   In Figure 9, sets of curves for Dt/a^2 for the values of these dimensionless parameters are

452   plotted, using effective diffusion radii that represent typical grain sizes for each mineral. These

19

453   values of radii a are 0.5 mm for quartz, 250 μm for rutile and titanite, and 50 μm for zircon. The

454   curves define the time-temperature limits under which initial Al, Si, Zr or Ti compositional

455   information will be preserved in the grain centers of each mineral, with concentrations at crystal

456   cores remaining unaltered for conditions below the curves, but affected by the surrounding

457   medium for conditions above the curves. These plots demonstrate that crystallization conditions

458   estimated from Al concentrations in rutile will be far more resistant to diffusional alteration than

459   those from the Zr-in-rutile thermometer. For example, at 900°C, Al compositional information

460   would be preserved over ~3 Gyr in the center of 250 μm radius rutile grains, but Zr

461   compositional information would be preserved for only about 300,000 years at this temperature.

462   Al-in-rutile compositions will also be much better preserved during subsolidus thermal events

463   subsequent to crystallization than those for Ti-in-quartz and Zr-in-titanite crystallization

464   thermometers. In general, the likelihood of preservation of Si concentrations in rutile falls

465   between that for Zr and Al.

466   The conclusions summarized above can be graphically illustrated in a manner that simulates

467   x-ray maps that could be obtained on individual rutile crystals in natural rocks. Concentration

468   contour maps are well-suited to portraying the spatial distribution (and therefore diffusion

469   progress) of elements in natural crystals, as a complement to the sometimes intuitively elusive

470   dimensionless quantity Dt/a^2. To this end, we ran simulations of Si, Al and Zr diffusion in rutile

471   crystals with the goal of contouring the resulting concentrations in 2-D section to illustrate and

472   compare results. In this case our model crystal was a cylindrical rutile grain 200 μm in diameter

473   and 600 μm long; calculations were performed using the CYLMOD computer program written

474   by Watson et al. (2010) for the purpose of modeling diffusion in finite cylinders. The

475   concentration of the elements was held constant at the cylinder surface at an arbitrary value

20

476   below the initial (uniform) concentration within the cylinder. The broad objective was to

477   illustrate outcomes for the three elements that span behaviors from nearly closed (very limited

478   diffusion) to badly compromised. An isothermal heating event lasting 10 million years was used

479   for this comparison; results are shown in Figure 10 as concentration contours within the rutile

480   cylinder expressed in terms of % of the initial uniform value. For the time span considered,

481   diffusion progress for Al, Si and Zr is approximately the same (and very limited) at 900, 700 and

482   500°C, respectively. The three diffusants also show similar progress (66-78% overall retention)

483   at 950, 800 and 600°C, respectively. Higher temperatures result pronounced open-system

484   behavior, as shown by the bottom row of panels in Figure 10.

485   All of the preceding discussion applies to isothermal conditions. Given the availability of

486   diffusion laws for the relevant elements, the possibility of open-system behavior during both

487   prograde and retrograde metamorphism can also be readily addressed. Resetting of

488   thermobarometers during geologic cooling can be evaluated qualitatively using the well-known

489   closure-temperature equation of Dodson (1973), which returns closure temperatures for Al, Si

490   and Zr in rutile of ~1050°C, ~930°C, and ~700°C for spherical grains of 250 μm radius cooling

491   at 10°C /Myr. Similarly, there may be instances where rutile crystallizes in a metabasite at

492   relatively low temperature and is subsequently heated with increasing metamorphic grade,

493   possibly resetting one or more thermobarometers. In this case it is instructive to explore both

494   center retention (defined as above), and diffusive "opening", which we define as a 1% diffusive

495   loss or gain of the element of interest — i.e., incipient open-system behavior. Diffusive

496   "opening" and center retention during linear heating of spherical grains are readily evaluated

497   using the generalized expression of Watson and Cherniak (2013):

498 $$T_{rt\%} = \frac{0.457 \cdot (E_a / R)}{\chi_h + \log\left[\dfrac{E_a \cdot D_0}{R \cdot dT / dt \cdot a^2}\right]}$$ (1)

499   where D_o and E_a are the Arrhenius parameters for the diffusant of interest, dT/dt is the heating

500   rate, a is the radius of the grain domain, R is the gas constant, and χ_h is a constant describing the

501   fraction of change in the amount. For a given heating trajectory, $T_{rt\%}$ is the temperature (in

502   kelvins) at which a specific fractional retention (or loss) is reached, and where the constant χ_h

503   will have a specific value depending on the amount of fractional loss. For retention levels of

504   50% and 99%, the center retention and diffusive opening criteria defined above, χ_h has values of

505   -0.785 and 2.756, respectively. In calculations, we use a linear heating rate of 10°C/Myr and plot

506   opening and center retention temperatures for Al as a function of grain radius in Figure 11. For

507   comparison, we also plot conditions for diffusive opening of both Zr and Pb in rutile, using the

508   diffusion parameters of Cherniak et al. (2007a) and Cherniak (2000) respectively. This provides

509   additional illustration of the comparatively high retentivity for Al chemical signatures in rutile;

510   for example, Al would require heating to temperatures in excess of 840°C to induce a 1% change

511   in Al composition in 100μm radius rutile grains, while comparable changes in Zr and Pb

512   compositions would result when reaching temperatures of only ~420°C and ~480°C,

513   respectively.

514

515   **Implications**

516   This study has shown that both Al and Si are among the slowest-diffusing species measured in

517   rutile to date. With these slow diffusivities, the recently-developed Al-in-rutile crystallization

518   geothermobarometer (Hoff and Watson, 2018) will be a robust indicator of past temperature and

519   pressure conditions, more resistant to diffusional alteration than the Zr-in-rutile crystallization

520   thermometer. In addition, should a Si-in-rutile thermometer become more fully developed, Si

521   concentrations in rutile will likewise provide a crystallization thermometer resistant to alteration

522   by diffusion.

523

528
529

530 **References**

531

532 Akse, J.R., and Whitehurst, H.B. (1978) Diffusion of titanium in slightly reduced rutile. Journal

533   of Physics and Chemistry of Solids, 39, 457-465.

534 Bak, T., Bogdanoff, P., Fiechter, S., and Nowotny, J. (2012) Defect engineering of titanium

535   dioxide: full defect disorder. Advances in Applied Ceramics, 111, 62-71.

536 Bak, T., Nowotny, J., Rekas, M., and Sorrell, C. (2003) Defect chemistry and semiconducting

537   properties of titanium dioxide. Journal of Physics and Chemistry of Solids, 64, 1057-1067.

538 Béjina, F., and Jaoul, O. (1997) Silicon diffusion in silicate minerals. Earth and Planetary

539   Science Letters, 153, 229-238.

540 Béjina, F., and Jaoul, O. (1996) Silicon self-diffusion in quartz and diopside measured by nuclear

541   micro-analysis methods. Physics of Earth and Planetary Interiors, 97, 145-162.

542 Boisvert, G., Lewis, L.J., and Yelon, A. (1995) Many-body nature of the Meyer-Neldel

543   compensation law for diffusion. Physical Review Letters, 75, 469-472.

544 Brenan, J.M., Shaw, H.F., Phinney, D.L., and Ryerson, F.J.,(1994) Rutile-aqueous fluid

545   partitioning of Nb, Ta, Hf, Zr, U and Th; implications for high field strength element

546   depletions in island-arc basalts. Earth and Planetary Science Letters, 128, 327-339.

547 Cherniak, D.J. (2008) Si diffusion in zircon. Physics and Chemistry of Minerals, 35, 179–187.

548 Cherniak, D.J. (2006) Zr diffusion in titanite. Contributions to Mineralogy and Petrology, 152,

549   639-647.

550 Cherniak, D.J. (2003) Silicon self-diffusion in single crystal natural quartz and feldspar. Earth

551   Earth and Planetary Science Letters, 214, 655-668.

552   Cherniak, D.J. (2000) Pb diffusion in rutile. Contributions to Mineralogy and Petrology, 139,

553   198-207.

554   Cherniak, D.J. (1995) Diffusion of Pb in plagioclase and K-feldspar measured by Rutherford

555   Backscattering spectroscopy and resonant nuclear reaction analysis. Contributions to

556   Mineralogy and Petrology,. 120, 358-371.

557   Cherniak, D.J. (1993) Lead diffusion in titanite and preliminary results on the effects of radiation

558   damage on Pb transport. Chemical Geology, 110, 177-194.

559   Cherniak, D.J., and Watson, E.B. (2007) Ti diffusion in zircon. Chemical Geology, 242, 473-

560   486.

561   Cherniak, D.J., and Watson, E.B. (1994) A study of strontium diffusion in plagioclase using

562   Rutherford Backscattering Spectroscopy, Geochimica et Cosmochimica Acta, 58, 5179-5190.

563   Cherniak, D.J., and Watson, E.B. (1992) A study of strontium diffusion in K-feldspar, Na-K

564   feldspar and anorthite using Rutherford Backscattering Spectroscopy. Earth and Planetary

565   Science Letters, 411-425.

566   Cherniak, D.J. Manchester, J., and Watson, E.B. (2007a) Zr and Hf diffusion in rutile. Earth and

567   Planetary Science Letters, 261, 267-279.

568   Cherniak, D.J., Watson, E.B., and Wark, D.A. (2007b) Ti diffusion in quartz, Chemical Geology,

569   236, 65-74.

570   Corfu, F., and Muir, T.L. (1989) The Hemlo-Heron Bay greenstone belt and Hemlo Au-Mo

571   deposit, Superior Province, Ontario, Canada; 2, Timing of metamorphism, alteration and Au

572   mineralization from titanite, rutile, and monazite U-Pb geochronology. Chemical Geology -

573   Isotope Geoscience, 79, 201-223.

574 Corfu, F., and Andrews, A.J. (1986) A U-Pb age for mineralized Nipissing Diabase, Gowganda,

575   Ontario. Canadian Journal of Earth Sciences. 23, 107-109.

576 Crank, J. (1975) The Mathematics of Diffusion (2nd ed.), Oxford, 414 pp.

577 Cruz-Uribe, A.M., Feineman, M.D., Zack, T., and Jacob, D.E. (2018) Assessing trace element

578   (dis)equilibrium and the application of single element thermometers in metamorphic rocks.

579   Lithos, 314–315, 1–15.

580 Davis, W.J. (1997) U-Pb zircon and rutile ages from granulite xenoliths in the Slave Province;

581   evidence for mafic magmatism in the lower crust coincident with Proterozoic dike swarms.

582   Geology, 25, 343-346.

583 Deer, W.A., Howie, R.A., and Zussman, J. (1992) An introduction to the rock-forming minerals.

584   Longman Scientific Technical, Harlow, United Kingdom.

585 Degeling, H.S. (2003) Zr equilibria in metamorphic rocks. Unpublished PhD thesis, Australian

586   National University, 231 pp.

587 Demiryont, H. (1985) Optical properties of SiO_2-TiO_2 composite films. Applied Optics 24,

588   2647-2650.

589 Dieckmann, R., Mason, T.O., Hodge, J.D., and Schmalzried, H. (1978) Defects and cation

590   diffusion in magnetite (III.) Tracer diffusion of foreign tracer cations as a function of

591   temperature and oxygen potential. Berichte der Bunsengesellschaft für Physikalische Chemie,

592   82, 778-783.

593 Dohmen, R., Chakraborty, S., and Becker, H.-W. (2002) Si and O diffusion in olivine and

594   implications for characterizing plastic flow in the mantle. Geophysical Research Letters, 29,

595   26-1 - 26-4.

596   Dohmen, R., Marschall, H.R., Ludwig, T., and Polednia, J. (2018) Diffusion of Zr, Hf, Nb and

597   Ta in rutile: effects of temperature, oxygen fugacity, and doping level, and relation to rutile

598   point defect chemistry. Physics and Chemistry of Minerals. https://doi.org/10.1007/s00269-

599   018-1005-7

600   Escudero, A., Langenhorst, F., and Müller, W.F. (2012) Aluminum solubility in TiO_2 rutile at

601   high pressure and experimental evidence for a $CaCl_2$-structured polymorph. American

602   Mineralogist, 97, 1075–1082.

603   Escudero, A., and Langenhorst, F. (2012) Incorporation of Si into TiO_2 phases at high pressure.

604   American Mineralogist, 97, 524-531.

605   Ewing, T.A., and Müntener, O. (2018) The mantle source of island arc magmatism during early

606   subduction: Evidence from Hf isotopes in rutile from the Jijal Complex (Kohistan arc,

607   Pakistan). Lithos, 308–309, 262–277.

608   Ewing, T.A., Hermann, J., and Rubatto, D. (2013) The robustness of the Zr-in-rutile and Ti-in-

609   zircon thermometers during high-temperature metamorphism (Ivrea-Verbano Zone, northern

610   Italy). Contributions to Mineralogy and Petrology, 165, 757–779.

611   Ferry, J.M., and Watson, E.B. (2007) New thermodynamic models and revised calibrations for

612   the Ti-in-zircon and Zr-in-rutile thermometers. Contributions to Mineralogy and Petrology,

613   154, 429-437.

614   Fielitz, P., Borchardt, G., Schmücker, M., and Schneider, H. (2006) Al-26 diffusion

615   measurement in 2/1-mullite by means of Secondary Ion Mass Spectrometry. Solid State

616   Ionics, 177, 493-496.

617 Foley, S.F., Barth, M.G., and Jenner, G.A. (2000) Rutile/melt partition coefficients for trace

618   elements and an assessment of the influence of rutile on the trace element characteristics of

619   subduction zone magmas. Geochimica et Cosmochimica Acta, 64, 933-938.

620 Gaetani, G.A., Asimow, P.D., and Stolper, E.M. (2008) A model for rutile saturation in silicate

621   melts with application to eclogite partial melting in subduction zones and mantle plumes.

622   Earth and Planetary Science Letters, 272, 720-729.

623 Gesenhues, U., and Rentschler, T. (1999) Crystal growth and defect structure of Al^{3+}-doped

624   rutile. Journal of Solid State Chemistry, 143, 210-218.

625 Gesenhues, U. (1997) Doping of TiO_2 pigments by Al^{3+}. Solid State Ionics, Diffusion &

626   Reactions, 101-103, 1171-80.

627 Golden, E.M., Giles, N.C., Shan Yang, and Halliburton, L.E. (2015) Interstitial silicon ions in

628   rutile TiO_2 crystals. Physical Review, B 91, 134110.

629 Gonzalez-Elipe, A.R., Gracia, F., Yubero, F., Holgado, J.P., Espinos, J.P., and Girardeau, T.

630   (2006) SiO_2/TiO_2 thin films with variable refractive index prepared by ion beam induced and

631   plasma enhanced chemical vapor deposition. Thin Solid Films, 500, 19-26.

632 Guo S., Tang P., Su B., Chen Y., Ye K., Zhang L., Gao Y., Liu J., and Yang Y. (2017) Unusual

633   replacement of Fe-Ti oxides by rutile during retrogression in amphibolite-hosted veins (Dabie

634   UHP Terrane); a mineralogical record of fluid-induced oxidation processes in exhumed UHP

635   slabs. American Mineralogist, 102, 2268-2283.

636 Hatta, K., Higuchi, M., Takahashi, J., and Kodaira, K. (1996) Floating zone growth and

637   characterization of aluminum-doped rutile single crystals. Journal of Crystal Growth, 163,

638   279-284.

639   Hayden, L.A., Watson, E.B., and Wark, D.A. (2008) A thermobarometer for sphene (titanite).

640   Contributions to Mineralogy and Petrology, 155, 529-540.

641   Heaman, L., and Parrish, R. (1991) U-Pb geochronology of accessory minerals. Short Course

642   Handbook, 19, 59-102. Mineralogical Association of Canada.

643   Hoff, C.M., and Watson, E.B. (2018) Aluminum in rutile as a recorder of temperature and

644   pressure. V.M. Goldschmidt Conference.

645   Hoshino, K., Peterson, N.L., and Wiley, C.L. (1985) Diffusion and point defects in TiO_{2-x}.

646   Journal of Physics and Chemistry of Solids, 46, 1397-1411.

647   Islam, M.M., Bredow, T., and Gerson, A. (2007) Electronic properties of oxygen-deficient and

648   aluminum-doped rutile TiO_2 from first principles. Physical Review, B 76, 045217.

649   Jaoul, O., Poumellec, M., Froidevaux, C., and Havette, A. (1981) Silicon diffusion in forsterite:

650   A new constraint for understanding mantle deformation. In: Anelasticity in the Earth, Stacey,

651   F.D., Paterson, M.S., Nicholas, A. (eds.), American Geophysical Union, pp. 95-100.

652   Jones, A. G. (2014) Compensation of the Meyer-Neldel Compensation Law for H diffusion in

653   minerals. Geochemistry Geophysics Geosystems, 15, doi:10.1002/2014GC005261

654   Karvinen, S. (2003) The effects of trace elements on the crystal properties of TiO_2. Solid State

655   Science, 5, 811-819.

656   Kohn, M.J., Penniston-Dorland, S.C., and Ferreira, J.C.S. (2016) Implications of near-rim

657   compositional zoning in rutile for geothermometry, geospeedometry, and trace element

658   equilibration. Contributions to Mineralogy and Petrology, 171, 78.

659   Le Gall, M., Lesage, B., and Bernardini, J. (1994) Self-diffusion in Al_2O_3. I. Aluminum diffusion

660   in single crystals. Philosophical Magazine, 70, 761–773.

29

661 Liu, L., Xiao, Y., Aulbach, S., Li, D., and Hou, Z. (2014) Vanadium and niobium behavior in

662   rutile as a function of oxygen fugacity: evidence from natural samples. Contributions to

663   Mineralogy and Petrology, 167, 1026.

664 Marschall, H.R., Dohmen, R., and Ludwig, T. (2013) Diffusion-induced fractionation of niobium

665   and tantalum during continental crust formation. Earth and Planetary Science Letters, 375,

666   361–371.

667 Marucco, J.-F., Gautron, J., and Lemasson, P. (1981) Thermogravimetric and electrical study of

668   nonstoichiometric titanium dioxide TiO_{2-x} between 800 and 1100°C. Journal of Physics and

669   Chemistry of Solids, 42, 363-367.

670 Mezger, K., Rawnsley, C.M., Bohlen, S.R., and Hanson, G.N. (1991) U-Pb garnet, sphene,

671   monazite, and rutile ages; implications for the duration of high-grade metamorphism and

672   cooling histories, Adirondack Mts., New York. Journal of Geology, 99, 415-428.

673 Mezger, K., Hanson, G.N., and Bohlen, S.R. (1989) High-precision U-Pb ages of metamorphic

674   rutile; application to the cooling history of high-grade terranes. Earth and Planetary Science

675   Letters, 96, 106-118.

676 Mitchell, R.J., and Harley, S.L. (2017) Zr-in-rutile resetting in aluminosilicate bearing ultra-high

677   temperature granulites: Refining the record of cooling and hydration in the Napier Complex,

678   Antarctica. Lithos, 272–273, 128–146.

679 Moore, D.K., Cherniak, D.J., and Watson, E.B. (1998) Oxygen diffusion in rutile from 750 to

680   1000 degrees C and 0.1 to 1000 MPa. American Mineralogist, 83, 700-711.

681 Morton, A.C., and Hallsworth, C.R. (1999) Processes controlling the composition of heavy

682   mineral assemblages in sandstones. Sedimentary Geology, 124, 3-30.

683   Mosenfelder, J.D., Kim, N., and Stebbins, J.F. (2010) Silicon coordination in rutile and TiO_2-II

684   at ambient and high pressures. American Mineralogist, 95, 968-973.

685   Nakayama, T., and Sasaki, T. (1963) The diffusion of barium in a rutile single crystal. Bulletin of

686   the Chemical Society of Japan, 36, 569-574.

687   Nowotny, M.K., Bak, T., and Nowotny, J. (2006a) Electrical properties and defect chemistry of

688   TiO_2 single crystal. III. Equilibrium kinetics and chemical diffusion. Journal of Physical

689   Chemistry, B 110, 16292-16301.

690   Nowotny, M.K., Bak, T., and Nowotny, J. (2006b) Electrical properties and defect chemistry of

691   TiO_2 single crystal. IV. Prolonged oxidation kinetics and chemical diffusion. Journal of

692   Physical Chemistry, B 110, 16302-16308.

693   Pape, J., Mezger, K., and Robyr, M. (2016) A systematic evaluation of the Zr-in-rutile

694   thermometer in ultra-high temperature (UHT) rocks. Contributions to Mineralogy and

695   Petrology, 171, 44.

696   Paladino, A. E., and Kingery, W. D. (1962) Aluminum ion diffusion in aluminum oxide. Journal

697   of Chemical Physics, 37, 957–962.

698   Ren, Y., Fei, Y., Yang, J., and Bai, W. (2009) SiO_2 solubility in rutile at high temperature and

699   high pressure. Journal of Earth Sciences, 20, 274-283.

700   Ryerson, F.J., and Watson, E.B. (1987) Rutile saturation in magmas; implications for Ti-Nb-Ta

701   depletion in island-arc basalts, Earth and Planetary Science Letters, 86, 225-239.

702   Sakaguchi, I., Yurimoto, H., and Sueno, S. (1992) Impurities dislocation diffusion in single

703   crystal MgO. Materials Science and Engineering, B 13, LI-L4.

704   Sasaki, J., Peterson, N.L., and Hoshino, K. (1985) Tracer impurity diffusion in single-crystal

705   rutile (TiO_{2-x}), Journal of Physics and Chemistry of Solids, 46, 1267-1283.

706   Schandl, E.S., Davis, D.W., and Krogh, T.E. (1990) Are the alteration halos of massive sulfide

707   deposits syngenetic? Evidence from U-Pb dating of hydrothermal rutile at the Kidd volcanic

708   center, Abitibi Subprovince, Canada. Geology, 18, 505-508.

709   Slepetys, R.A., and Vaughan, P.A. (1969) Solid solution of aluminum oxide in rutile titanium

710   oxide. Journal of Physical Chemistry, 73, 2157–2162.

711   Smye, A.J., and Stockli, D.F. (2014) Rutile U–Pb age depth profiling: A continuous record of

712   lithospheric thermal evolution. Earth and Planetary Science Letters, 408, 171–182.

713   Stalder, R., Foley, S.F., Brey, G.P., and Horn, I. (1998) Mineral-aqueous fluid partitioning of

714   trace elements at 900-1200 degrees C and 3.0-5.7 GPa; new experimental data for garnet,

715   clinopyroxene, and rutile, and implications for mantle metasomatism. Geochimica et

716   Cosmochimica Acta, 62, 1781-1801.

717   Stebbins, J.F. (2007) Aluminum substitution in rutile titanium dioxide: New constraints from

718   high-resolution ^{27}Al NMR. Chemistry of Materials, 19, 1862-1869.

719   Tailby, N.D., Cherniak, D.J., and Watson, E.B. (2018) Al diffusion in quartz. American

720   Mineralogist, 103, 839–847.

721   Taylor-Jones, K., and Powell, R. (2015). Interpreting zirconium-in-rutile thermometric results.

722   Journal of Metamorphic Geology, 33, 115–122.

723   Thomas, J.B., Watson, E.B., Spear, F.S., Shemella, P.T., Nayak, S.K., and Lanzirotti, A. (2010)

724   TitaniQ under pressure: the effect of pressure and temperature on the solubility of Ti in

725   quartz. Contributions to Mineralogy and Petrology, 160, 743-759.

726   Tomkins, H.S., Powell, R., and Ellis, D.J. (2007) The pressure dependence of the zirconium-in-

727   rutile thermometer. Journal of Metamorphic Geology, 25, 703-713.

728   Tual, L., Möller, C., and Whitehouse, M.J. (2018) Tracking the prograde P–T path of

729   Precambrian eclogite using Ti-in quartz and Zr-in-rutile geothermobarometry. Contributions

730   to Mineralogy and Petrology, 173, 56.

731   Van Orman, J.A., Li, C., and Crispin, K.L. (2009) Aluminum diffusion and Al-vacancy

732   association in periclase. Physics of Earth and Planetary Interiors, 172, 34-42.

733   Venkatu, D.A. and Poteat, L.E. (1970) Diffusion of titanium in single crystal rutile. Materials

734   Science and Engineering, 5, 258-562.

735   Vlassopoulos, D., Rossman, G.R., and Haggerty, S.E. (1993) Coupled substitution of H and

736   minor elements in rutile and the implications of high OH contents in Nb- and Cr-rich rutile

737   from the upper mantle. American Mineralogist, 78, 1181-1191.

738   Wark, D.A., and Watson, E.B. (2006) TitaniQ: A titanium-in-quartz geothermometer,

739   Contributions to Mineralogy and Petrology, 152, 743-754.

740   Watson, E.B., and Harrison, T.M. (2005) Zircon thermometer reveals minimum melting

741   conditions on earliest Earth. Science 308, 841-844.

742   Watson, E.B., and Cherniak, D.J. (2013) Simple equations for diffusion in response to heating.

743   Chemical Geology, 335, 93-104.

744   Watson, E.B., Wark, D.A., and Thomas, J.B. (2006) Crystallization thermometers for zircon and

745   rutile, Contributions to Mineralogy and Petrology, 151, 413-433.

746   Watson, E.B., Wanser, K.H., and Farley, K.A. (2010) Anisotropic diffusion in a finite cylinder,

747   with geochemical applications. Geochimica et Cosmochimica Acta, 74, 614-633.

748   Wong, L., Davis, D.W., Krogh, T.E., and Robert, F. (1991) U-Pb zircon and rutile chronology of

749   Archean greenstone formation and gold mineralisation in the Val d'Or region, Quebec. Earth

750   and Planetary Science Letters, 104, 325-336.

751   Yamazaki, D., Kato, T., Yurimoto, H., Ohtani, E., and Toriumi, M. (2000) Silicon self-diffusion

752   in MgSiO$_3$ perovskite at 25 GPa. Physics of Earth and Planetary Interiors, 119, 299-309.

753   Zack, T., Kronz, A., Foley, S.F., and Rivers, T. (2002) Trace element abundances in rutiles from

754   eclogites and associated garnet mica schists. Chemical Geology, 184, 97-122.

755   Zack, T., von Eynatten, H., Kronz, A. (2004a). Rutile geochemistry and its potential use in

756   quantitative provenance studies. Sedimentary Geology 171, 37–58.

757   Zack, T., Moraes, R., and Kronz, A. (2004b) Temperature dependence of Zr in rutile: empirical

758   calibration of a rutile thermometer. Contributions to Mineralogy and Petrology, 148, 471-488.

759   Zener, C. (1952) Theory of diffusion. In: Shockley, W., Hollomon, J.H., Maurer, R., and Seitz,

760   F. (eds.), Imperfections in Nearly Perfect Crystals, Wiley, New York, pp. 289-314.

761   Zhu, L., Ackland, G., Hu, Q.-M., Zhou, J., and Sun, Z. (2017) Origin of the abnormal diffusion

762   of transition metal atoms in rutile. Physical Review, B 95, 245201.

763   Zhukova, I., O'Neill, H., and Campbell, I.H. (2017) A subsidiary fast‑diffusing substitution

764   mechanism of Al in forsterite investigated using diffusion experiments under controlled

765   thermodynamic conditions. Contributions to Mineralogy and Petrology, 172, 53.

766   Ziegler, J.F., and Biersack, J.P. (2006) The stopping and range of ions in matter. Computer code

767   SRIM 2006, http://www.srim.org.

768
769
770
771
772
773

774   Table 1. Trace and minor element compositions of rutile
775   from LA-ICPMS analyses

Element (ppm)	Natural Rutile (PA)	Synthetic Rutile
Al	330 ± 25	26 ± 9
V	1326 ± 32	--
Cr	538 ± 24	--
Fe	3063 ± 220	8 ± 4
Ni	279 ± 26	--
Zr	113 ± 6	--
Nb	2738 ± 101	--
Hf	5.9 ± 0.3	--
Ta	119 ± 3	--
W	65 ± 3	--

776
777

778

779

780

781 Table 2. Al Diffusion in Rutile

	$T(^oC)$	time(sec)	$D(m^2sec^{-1})$	log D	+/-	buffer	$C_o^{\dagger}$	source*
normal to (001):								
RuAl-11	1100	$1.72x10^6$	$3.78x10^{-23}$	-22.42	0.41	NNO	0.69	10:1
RuAl-7	1151	$9.43x10^5$	$3.93x10^{-22}$	-21.41	0.17	NNO	3.91	3:1
RuAl-10	1150	$7.83x10^5$	$3.84x10^{-22}$	-21.42	0.34	NNO	0.73	10:1
RuAl-24	1150	$3.51x10^5$	$1.99x10^{-21}$	-20.70	0.16	IW	3.81	10:1
RuAl-1	1200	$4.28x10^5$	$1.64x10^{-21}$	-20.78	0.18	UB	6.89	3:1
RuAl-2	1200	$2.59x10^5$	$2.26x10^{-21}$	-20.65	0.16	NNO	5.71	3:1
RuAl-9	1200	$4.18x10^5$	$1.76x10^{-21}$	-20.75	0.25	NNO	1.05	10:1
RuAl-20	1200	$2.59x10^5$	$1.30x10^{-21}$	-20.89	0.17	NNO	5.64	10:1 + Nb
RuAl-3	1250	$1.67x10^5$	$7.38x10^{-21}$	-20.13	0.15	NNO	7.65	3:1
RuAl-16	1250	$8.64x10^4$	$1.02x10^{-20}$	-19.99	0.14	NNO	3.81	10:1
RuAl-12	1250	$1.66x10^5$	$8.01x10^{-21}$	-20.10	0.11	NNO	4.60	10:1
RuAl-15	1250	$5.45x10^5$	$6.48x10^{-21}$	-20.19	0.13	NNO	1.42	10:1
RuAl-19	1250	$2.02x10^5$	$9.33x10^{-21}$	-20.03	0.10	UB	2.02	Al_2O_3
RuAl-23	1250	$5.45x10^5$	$2.03x10^{-20}$	-19.69	0.08	IW	5.16	10:1
RuAl-4	1300	$6.84x10^4$	$2.89x10^{-20}$	-19.54	0.13	NNO	9.97	3:1
RuAl-13	1300	$9.24x10^4$	$2.87x10^{-20}$	-19.54	0.12	NNO	3.70	10:1
RuAl-6	1350	$5.04x10^4$	$7.12x10^{-20}$	-19.15	0.16	NNO	7.65	3:1
RuAl-14	1350	$5.40x10^4$	$6.18x10^{-20}$	-19.21	0.12	NNO	4.05	10:1
RuAl-22	1350	$6.12x10^4$	$2.22x10^{-19}$	-18.65	0.08	IW	7.13	10:1
RuAl-5	1400	$1.80x10^4$	$5.50x10^{-19}$	-18.26	0.26	NNO	4.50	3:1
(100)								
RuAl-17	1200	$3.35x10^5$	$2.14x10^{-21}$	-20.67	0.16	NNO	1.07	10:1
RuAl-18	1300	$7.56x10^4$	$4.89x10^{-20}$	-19.31	0.23	NNO	1.14	10:1

784 * 3:1 - 3:1 ratio (by wt.) TiO_2: Al_2O_3; 10:1 - 10:1 ratio (by wt.) TiO_2:Al_2O_3

785 † surface concentration in at. percent

786

36

787 Table 3. Si Diffusion in Rutile

	$T(^oC)$	time(sec)	$D(m^2sec^{-1})$	log D	+/-	buffer	$C_o^{\dagger}$	source
normal to (001):								
RuSi-38	1100	$9.49x10^5$	$2.02x10^{-22}$	-21.69	0.40	NNO	0.63	diff couple
RuSi-11	1149	$9.50x10^5$	$5.50x10^{-22}$	-21.26	0.34	UB	1.89	$TiO_2:SiO_2$
RuSi-34	1151	$5.11x10^5$	$6.76x10^{-22}$	-21.17	0.39	NNO	0.99	diff couple
RuSi-42	1150	$3.51x10^5$	$2.92x10^{-21}$	-20.53	0.17	IW	3.81	diff couple
RuSi-1	1200	$3.53x10^5$	$6.39x10^{-22}$	-21.19	0.35	UB	1.09	SiO_2
RuSi-31	1200	$2.82x10^5$	$1.56x10^{-21}$	-20.81	0.34	UB	0.69	diff couple
RuSi-32	1200	$2.48x10^5$	$1.52x10^{-21}$	-20.82	0.23	NNO	1.73	diff couple
RuSi-2	1250	$1.98x10^5$	$1.30x10^{-21}$	-20.88	0.20	UB	1.74	SiO_2
RuSi-37	1250	$2.45x10^5$	$9.36x10^{-22}$	-21.03	0.21	NNO	4.15	diff couple
RuSi-41	1250	$2.56x10^5$	$1.31x10^{-20}$	-19.88	0.20	IW	2.99	diff couple
RuSi-3	1301	$7.56x10^4$	$3.36x10^{-21}$	-20.47	0.20	UB	1.66	SiO_2
RuSi-4	1301	$6.84x10^4$	$3.97x10^{-21}$	-20.40	0.31	UB	1.15	$TiO_2:SiO_2$
RuSi-20	1299	$5.83x10^5$	$2.15x10^{-21}$	-20.67	0.18	UB	3.46	$TiO_2:SiO_2$
RuSi-21	1299	$2.54x10^5$	$2.43x10^{-21}$	-20.61	0.18	UB	3.34	$TiO_2:SiO_2$
RuSi-28	1300	$8.64x10^4$	$8.85x10^{-21}$	-20.05	0.29	UB	0.94	SiO_2
RuSi-35	1300	$8.64x10^4$	$2.30x10^{-21}$	-20.64	0.44	NNO	2.19	diff couple
RuSi-7	1351	$5.76x10^4$	$8.23x10^{-21}$	-20.08	0.18	UB	4.12	$TiO_2:SiO_2$
RuSi-36	1350	$7.56x10^4$	$3.79x10^{-21}$	-20.42	0.14	NNO	7.17	diff couple
RuSi-40	1350	$7.56x10^4$	$4.41x10^{-20}$	-19.36	0.27	IW	1.40	diff couple
RuSi-6	1400	$1.44x10^4$	$1.19x10^{-20}$	-19.92	0.20	UB	4.88	$TiO_2:SiO_2$
RuSi-39	1400	$1.44x10^4$	$1.78x10^{-20}$	-19.75	0.29	NNO	4.98	diff couple
RuSi-8	1450	$7.20x10^3$	$2.22x10^{-20}$	-19.65	0.19	UB	8.96	$TiO_2:SiO_2$
normal to (100):								
RuSi-10	1200	$3.46x10^5$	$4.80x10^{-22}$	-21.32	0.29	UB	0.77	$TiO_2:SiO_2$
RuSi-13	1299	$9.00x10^4$	$5.00x10^{-21}$	-20.30	0.30	UB	0.64	$TiO_2:SiO_2$
RuSi-19	1399	$5.94x10^4$	$1.22x10^{-20}$	-19.91	0.28	UB	1.19	$TiO_2:SiO_2$
natural rutile, cut parallel to c:								
NRuSi-9	1150	$4.28x10^5$	$3.26x10^{-22}$	-21.49	0.46	NNO	0.95	diff couple
NRuSi-8	1250	$6.48x10^4$	$3.02x10^{-21}$	-20.52	0.38	NNO	0.96	diff couple
NRuSi-10	1350	$1.62x10^4$	$1.35x10^{-20}$	-19.87	0.18	NNO	4.78	diff couple

791 † surface concentration in at. percent

792
793
794

37

795 **Captions for figures**

796 Figure 1. Example Al (a) and Si (b) diffusion profiles for rutile. The Al experiment (on synthetic

797 rutile, with diffusion normal to (001)) was run at 1400°C for 5h. Profiles from both RBS and

798 NRA, using the $^{27}Al(p,\gamma)^{28}Si$ reaction, are plotted. The Si profiles are from an experiment on

799 synthetic rutile run at 1350°C for 16h (grey symbols), and for an experiment on natural rutile run

800 for 4.5h at 1350°C (white symbols).

801

802 Figure 2. Arrhenius plot of Al diffusion data for rutile. For diffusion normal to (001), for

803 experiments buffered at NNO, we obtain an activation energy of 531 ± 27 kJ mol^{-1} and pre-

804 exponential factor of 1.21×10^{-2} m^{2}s^{-1} (log D$_o$ = -1.92 ± 0.92). There appears to be little

805 anisotropy when comparing diffusion normal to (001) and (100). Diffusion under IW-buffered

806 conditions is faster by about half a log unit.

807

808 Figure 3. Arrhenius plot of Si diffusion data for synthetic and natural rutile. For Si diffusion

809 perpendicular to (001) in synthetic rutile under unbuffered conditions, we obtain an activation

810 energy of 275 ± 45 kJ mol^{-1} and a pre-exponential factor 4.41×10^{-12} m^{2}s^{-1} (log D$_o$ = -11.36 ±

811 1.38). There is little evidence of diffusional anisotropy when comparing diffusivities normal to

812 (100) and (001). For diffusion under NNO-buffered conditions in synthetic rutile, normal to

813 (001), an activation energy of 216 ± 48 kJ mol^{-1} and a pre-exponential factor 4.07×10^{-14} m^{2}s^{-1}

814 (log D$_o$ = -13.39 ± 1.62) are obtained; a fit to both the NNO- buffered and unbuffered data results

815 in an activation energy of 254 ± 31 kJ mol^{-1} and a pre-exponential factor 8.53×10^{-13} m^{2}s^{-1} (log D$_o$

816 = -12.07 ± 1.03). Diffusivities of Si in natural rutile under NNO-buffered conditions do not differ

817 significantly from those obtained for NNO-buffered synthetic rutile, indicating that differences in

38

818   trace and minor element compositions between the synthetic and natural materials have little

819   effect on diffusion. Like Al, Si diffusion exhibits a negative dependence on oxygen fugacity;

820   diffusivities under IW-buffered conditions are ~three quarters of a log unit faster than under

821   NNO-buffered conditions.

822

823   Figure 4. Time series for Al (a) and Si (b) at 1250°C and 1300°C, respectively. For both

824   elements, diffusivities are quite similar over times varying by more than a factor of 6, suggesting

825   that volume diffusion is the dominant contributor to the observed diffusion profiles.

826

827   Figure 5. Selected cation diffusion data for rutile. Sources for data: Cr, Fe - Sasaki et al. (1985);

828   Ti- Akse and Whitehurst, 1978; Nb, Ta - Marschall et al. (2013); Hf, Zr - Cherniak et al (2007);

829   Pb - Cherniak (2000); Al, Si - this study.

830

831   Figure 6. (a) Al diffusion data for selected minerals. Sources for data: quartz - Tailby et al.,

832   2018; forsterite - Zhukova et al., 2017; MgO - Van Orman et al., 2009; Al_2O_3 - LeGall et al.,

833   1994; Paladino and Kingery, 1962; magnetite - Dieckmann et al. 1978; mullite - Fielitz et al.,

834   2006. (b) Si diffusion data for selected minerals. Sources for data: quartz, anorthite, labradorite -

835   Cherniak, 2003; zircon - Cherniak, 2008; forsterite - Jaoul et al., 1981; olivine - Dohmen et al,

836   2002; MgO - Sakaguchi et al., 1992; diopside - Béjina and Jaoul, 1996; perovskite - Yamazaki et

837   al. , 2000.

838

839   Figure 7. Plot of activation energy (in kJ mol^{-1}) vs. the log of the pre-exponential factor D_o,

840   showing that Si diffusion data for silicates conform well to the linear 'diffusion compensation'

39

841   relation outlined by Bejina and Jaoul (1997) and Cherniak (2008). The compensation line can be

842   described by the equation $E = 647.7 + 30.5*\log D_o$. Data plotted are from Bejina and Jaoul

843   (1997) and Cherniak (2008). Results for Si diffusion in rutile from the present study (dark

844   squares) are also plotted. These fall closely along the diffusion compensation trend, as does that

845   for Si diffusion in MgO (white square).

846

847   Figure 8. Summary of data for diffusion of mineral-element pairs employed in selected

848   crystallization geothermometers. Sources for data: Ti - zircon: Cherniak and Watson (2007); Zr

849   - rutile: Cherniak et al. (2007a); Zr- titanite; Cherniak (2006); Ti - quartz: Cherniak et al.

850   (2007b); Al - rutile: this study.

851

852   Figure 9. Curves representing time-temperature conditions for mineral-element pairs used in

853   crystallization thermometers under which Ti, Zr, Al or Si signatures at the center of grains will

854   be lost. For times and temperatures below the curves, concentrations at crystal cores will remain

855   unaffected, but will be influenced by the surrounding medium when conditions above the curves

856   apply. In calculations, diffusivities from the Arrhenius relations plotted in Figure 8 are used, and

857   effective diffusion radii differing with mineral type are selected to reflect grain sizes typical for

858   each mineral: 50 μm for zircon, 0.5 mm for quartz, and 250 μm for both rutile and titanite. Rutile

859   will be considerably more retentive of Al compositions at grain centers than Zr; for example, at

860   900°C, Zr signatures would be altered in times of ~ 300,000 years, while Al signatures would be

861   preserved at this temperature over times on order 3 billion years.

862

863 Figure 10. Results of diffusion calculations for a cylindrical model rutile crystal 200 μm in

864 diameter and 600 μm long. The cylinder axis (dashed line) lies in the plane of the panels, which

865 are contoured to show the diffusional response of Si, Al and Zr at the temperatures indicated for

866 a holding time of 10 million years. Contours represent % retention of the original element

867 concentration at a given axial and radial location within the crystal. The contour interval is 10%;

868 the innermost contour represents 90% retention except where indicated otherwise. F is the

869 fraction of the element retained in the bulk crystal. The three temperatures modeled for each

870 element were chosen to show the transition from essentially closed-system behavior (F > 0.9; top

871 row) to severely compromised elemental concentrations (bottom row). See text for details.

872

873 Figure 11. Conditions for diffusive "opening" (defined as loss of 1% of the diffusant) and center

874 retention (equivalent to preservation of initial composition at grain center, but 50% loss of

875 diffusant) for Al, Pb, Si and Zr in rutile in the case of linear heating. Calculations are performed

876 using equation 1, a linear heating rate of 10°C/Ma, the appropriate values of the constant χ_h for

877 each criterion, and the diffusion parameters plotted in Figure 5. These calculations again

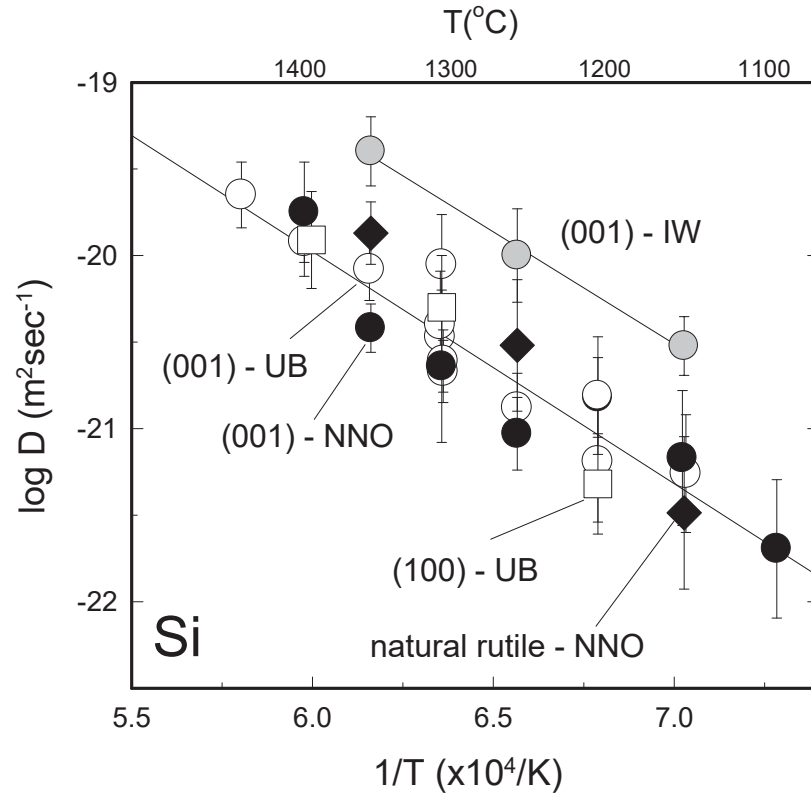878 illustrate the relative robustness of Al chemical signatures in rutile.
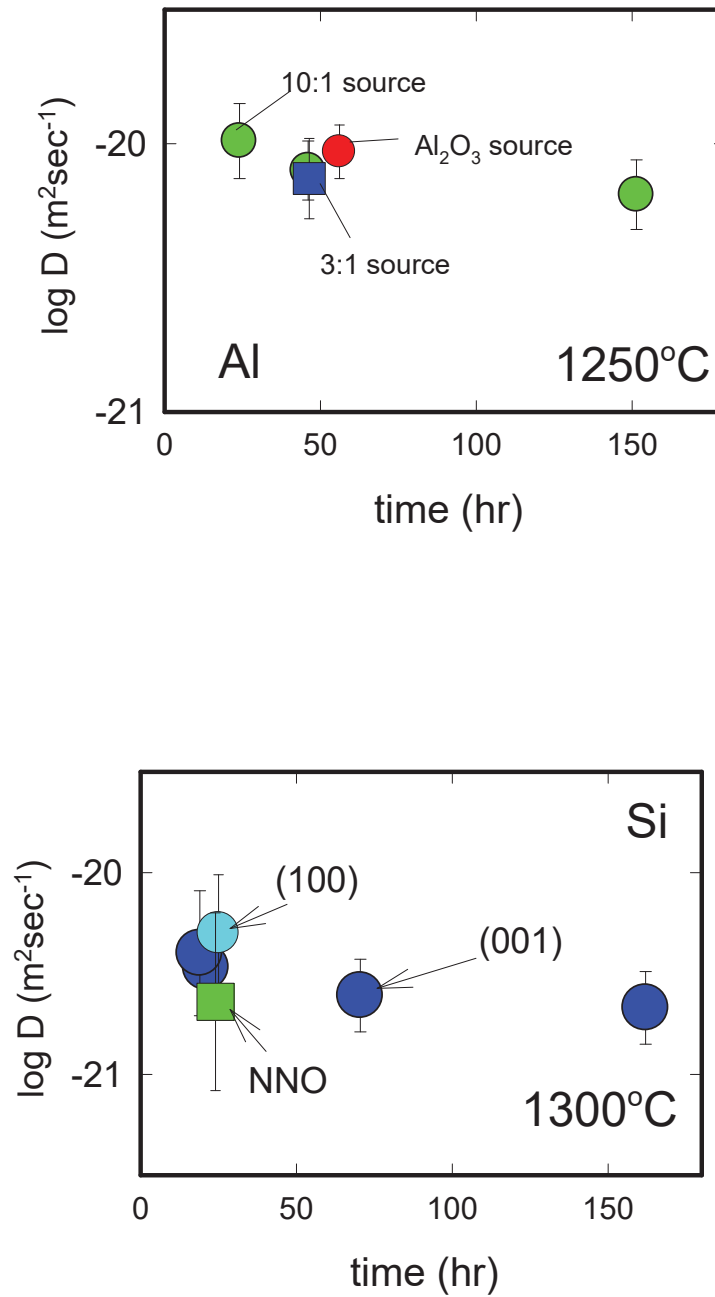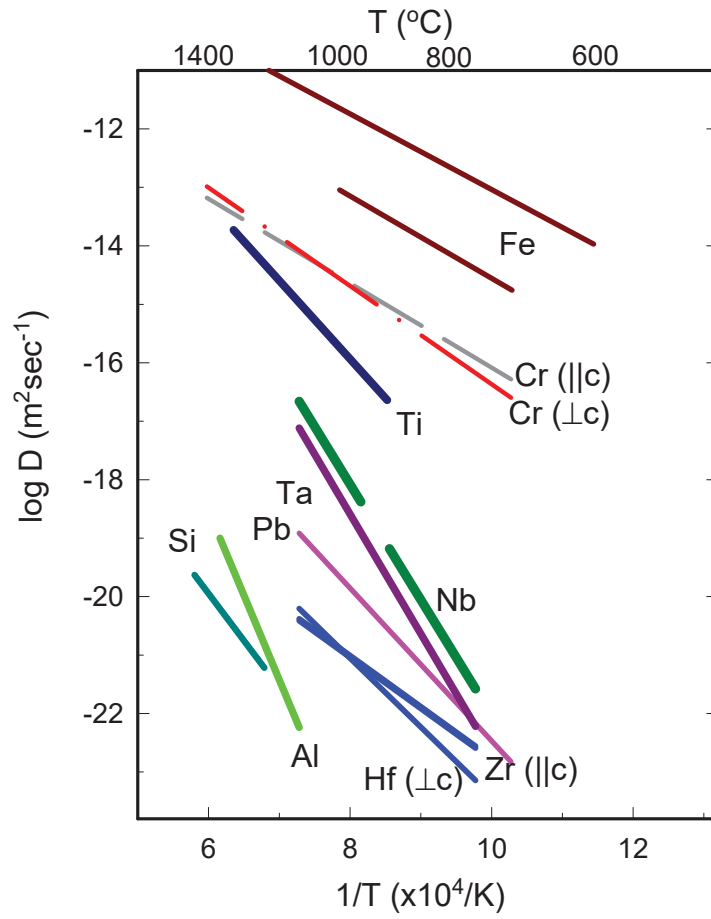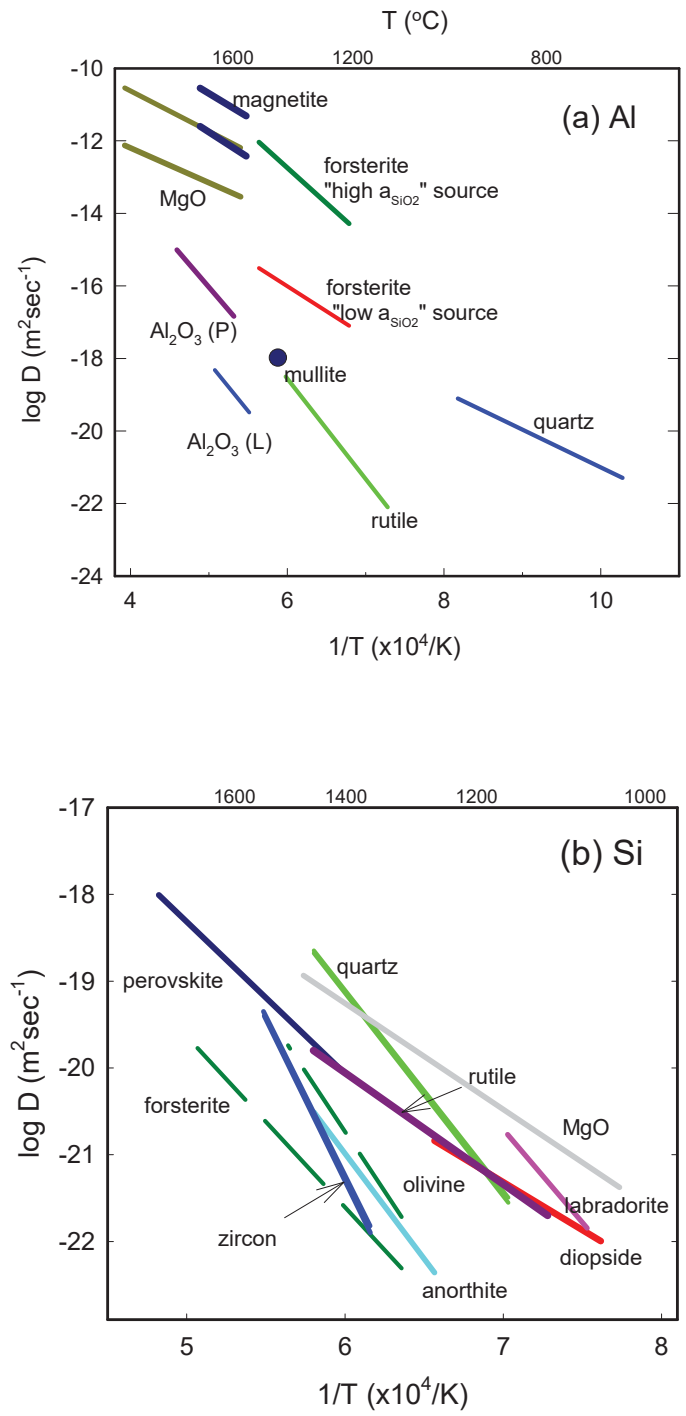
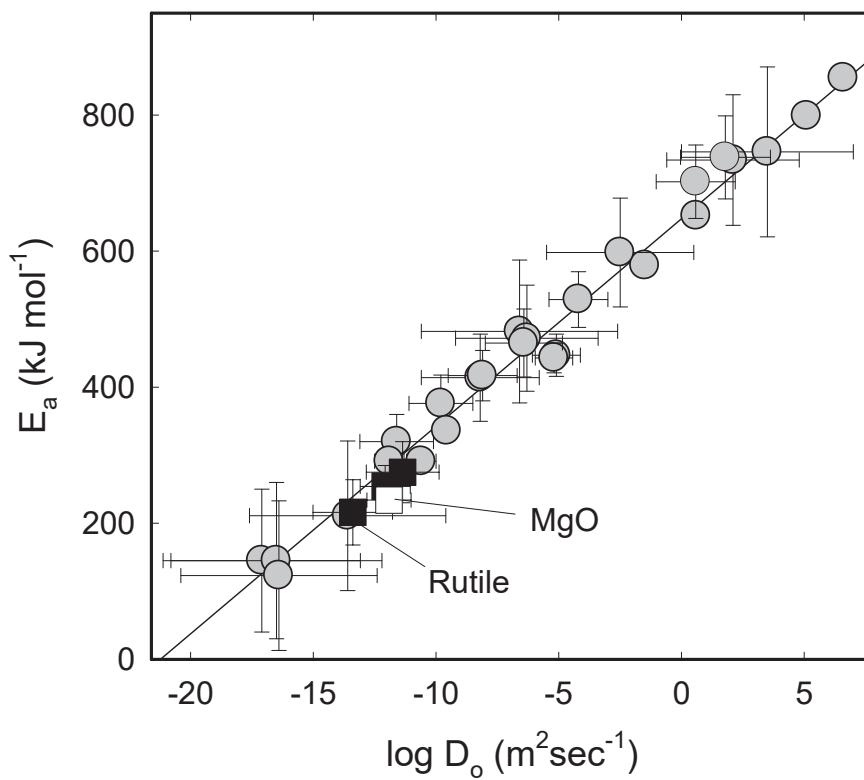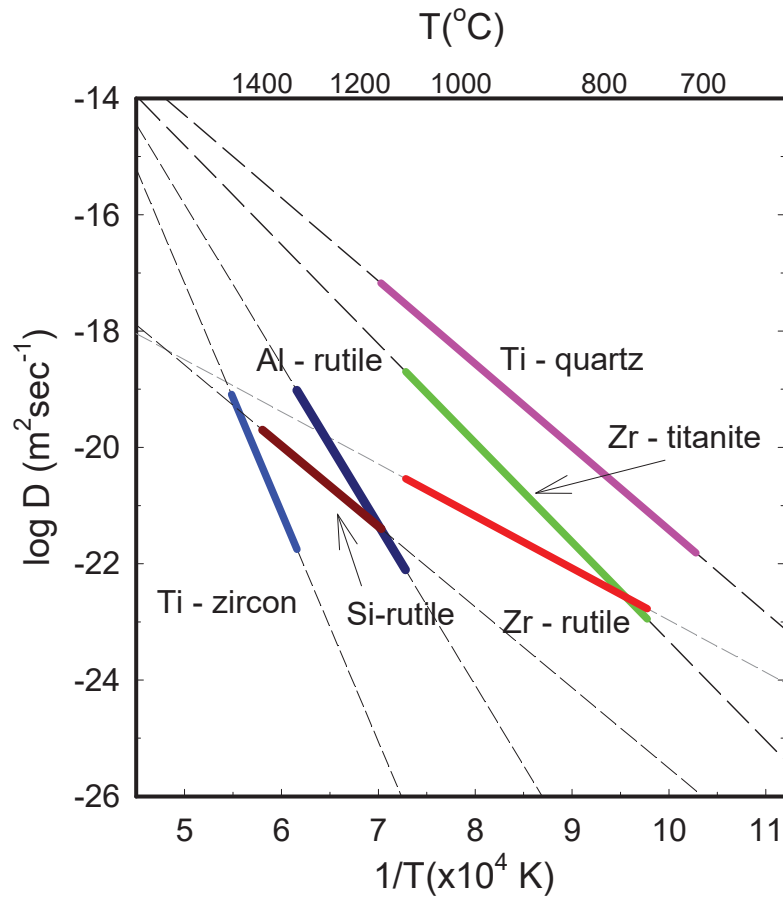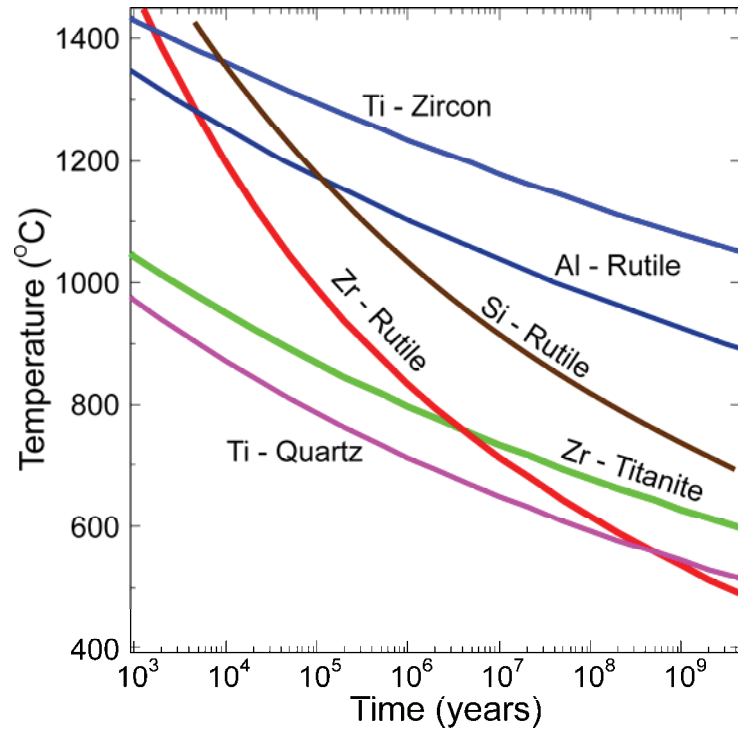879

Figure 1
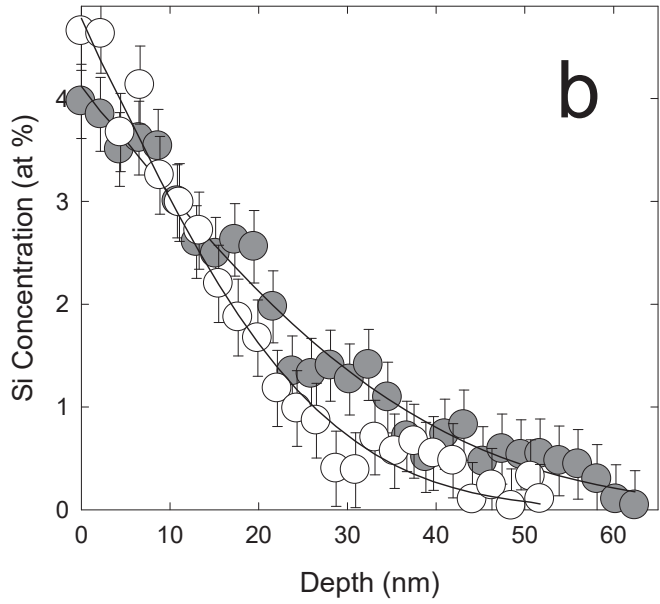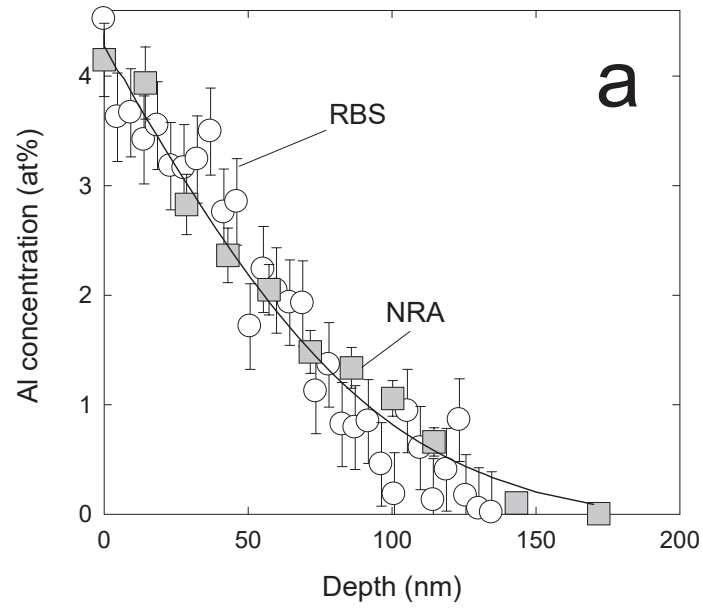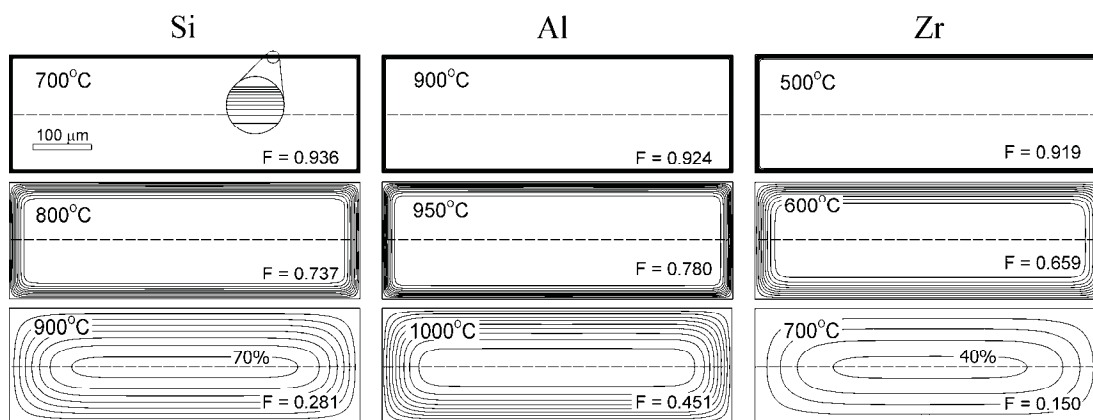
Figure 2
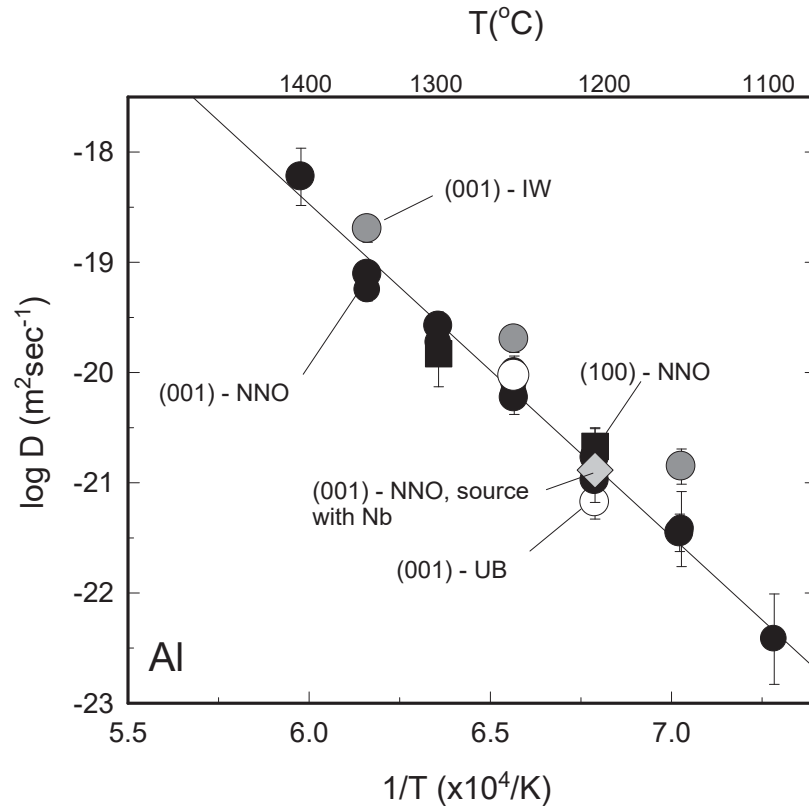
Figure 3

Figure 4

Figure 5

Figure 6

Figure 7

Figure 8

Figure 9

Figure 10

Figure 11